



# Axial resolution improvement of two-photon microscopy by multi-frame reconstruction and adaptive optics

SHIWEI YE,<sup>1,2</sup> YIXUAN YIN,<sup>1,2</sup> JING YAO,<sup>1,2</sup> JUN NIE,<sup>3</sup> YUCHEN SONG,<sup>1,4</sup> YUFENG GAO,<sup>1,2</sup> JIA YU,<sup>1,2</sup> HUI LI,<sup>1,2</sup> PENG FEI,<sup>3,5</sup> AND WEI ZHENG<sup>1,2,6</sup>

<sup>1</sup>Research Laboratory for Biomedical Optics and Molecular Imaging, Shenzhen Institutes of Advanced Technology, Chinese Academy of Sciences, Shenzhen 518055, China

<sup>2</sup>CAS Key Laboratory of Health Informatics, Shenzhen Institutes of Advanced Technology, Chinese Academy of Sciences, Shenzhen 518055, China

<sup>3</sup>School of Optical and Electronic Information, Huazhong University of Science and Technology, Wuhan 430074, China

<sup>4</sup>Department of Biomedical Engineering, The Hong Kong Polytechnic University, Hong Kong SAR, China

<sup>5</sup>feipeng@hust.edu.cn

<sup>6</sup>zhengwei@siat.ac.cn

**Abstract:** Two-photon microscopy (TPM) has been widely used in biological imaging owing to its intrinsic optical sectioning and deep penetration abilities. However, the conventional TPM suffers from poor axial resolution, which makes it difficult to recognize some three-dimensional fine features. We present multi-frame reconstruction two-photon microscopy (MR-TPM) using a liquid lens as a fast axial scanning engine. A sensorless adaptive optics (AO) approach is adopted to correct the aberrations caused by both the liquid lens and the optical system. By overcoming the effect of optical aberrations, inadequate sampling, and poor focusing capability of a conventional TPM, the axial resolution can be improved by a factor of 3 with a high signal-to-noise ratio. The proposed technology is compatible with the conventional TPM and requires no optical post-processing. We demonstrate the proposed method by imaging fluorescent beads, *in vitro* imaging of the neural circuit of mouse brain slice, and *in vivo* time-lapse imaging of the morphological changes of microglial cells in septic mice model. The results suggest that the axon of the neural circuit and the process of microglia along the axial direction, which cannot be resolved using conventional TPM, become distinguishable using the proposed AO MR-TPM.

© 2020 Optical Society of America under the terms of the [OSA Open Access Publishing Agreement](#)

## 1. Introduction

Fluorescence microscopy has revolutionized biomedical research in the past few decades. The sharp contrast, high speed, easy operation, and molecular specificity of fluorescence microscopy make it a powerful and versatile research tool, enabling its applications in fields ranging from cell biology to neuroscience. Among the fluorescence microscopy methods, two-photon excitation fluorescence microscopy (TPM) has attracted considerable attention owing to its submicron lateral resolution, intrinsic optical sectioning, and deep penetration abilities. TPM facilitates the observation of cellular and subcellular dynamics and can be used in deep live tissues within highly complex and heterogeneous environments such as the mammalian brain [1–3], thereby providing critical *in situ* and *in vivo* information. However, the axial resolution of TPM is usually limited to several micrometers and is significantly lower than the lateral resolution [4,5], which makes it difficult to recognize some three-dimensional (3D) fine features, e.g., dendrites, axons, and synapses along the axial direction. These problems hinder the further use of TPM in neuroscience studies.

Some technologies have been proposed to improve the axial resolution of TPM. Combined with the 4Pi technology, TPM can achieve submicron axial resolution. Because the 4Pi technology uses a superposition of two coherent wavefronts emanating from opposing objective lenses, it can effectively reduce the bandwidth of the point spread function (PSF) [6,7]. However, owing to its dependence on optical interference, the 4Pi TPM is restricted to transparent and thin biological samples, which makes it almost impossible to measure the structural and functional information from turbid samples such as the mouse brain *in vivo*. If combined with stimulated emission depletion (STED), TPM can break the diffraction limit in both the lateral and axial directions [8,9]. STED-TPM exploits a pair of focused laser beams: one for two-photon excitation and the other for the depletion of the fluorescence signal outside the two-photon excitation spot. Therefore, only fluorophores from the central part of the two-photon excitation spot are able to emit spontaneous fluorescence, and the spatial resolution is improved compared with the conventional TPM. Although STED-TPM can be used for *in vivo* imaging, it requires a sophisticated design of excitation paths, including both the two-photon excitation and STED paths, and strong light intensities. These requirements limit its applications for time-lapse imaging of live samples. Point-scanning structured illumination microscopy (SIM) [10] can be used to improve the spatial resolution of TPM by combining information from excitation and emission PSFs, such as two-photon multifocal SIM [11] and two-photon instant SIM [12,13]. Nevertheless, these technologies enable superior spatial resolutions at the expense of sophisticated computational or optical post-processing.

Multi-frame super-resolution technology, which utilizes many spatially related low-resolution images to reconstruct an output with a significantly high resolution, can be a potential approach to improve the axial resolution [14,15]. Multi-frame super resolution can effectively overcome the inadequate sampling and poor focusing capability of the poor axial resolution in far-field (lens-based) imaging. Moreover, multi-frame super resolution can break the diffraction limit and provide super-imaging capabilities without requiring significant modification of the hardware system. Based on this scheme, pixel super-resolution technology [16,17] and subvoxel light-sheet microscopy [18,19] have been developed for enhancing spatial resolution. However, to the best of our knowledge, few studies have been published on the use the multi-frame super resolution scheme to improve the resolution of TPM, in particularly, the axial resolution enhancement in volumetric imaging. Furthermore, the multi-frame super-resolution technology requires over-sampling measurements, whereas the mechanical movement used in the existing techniques restricts the experimental efficiency.

In this study, we propose multi-frame reconstruction two-photon microscopy (MR-TPM) with adaptive optics (AO) correction. This approach enables an almost threefold enhancement of the axial resolution relative to the conventional TPM. A liquid lens [20–22] is used as a fast axial scanning engine to alleviate the problem of low measurement efficiency. In addition, we utilized sensorless AO [23–25] to correct the aberrations introduced by both the liquid lens and the optical setup to improve the performance of two-photon images. Our method not only offers improved axial resolution for *in vivo* imaging but is also compatible with the conventional TPM and does not require optical post-processing. The capacity of AO MR-TPM is verified by imaging various samples, such as 200-nm fluorescent beads, the neural circuit of the Thy1-GFP-M mouse brain slice, and cerebral microglia of the live CX3CR1-GFP mouse.

## 2. Materials and methods

### 2.1. Optical setup

The schematic of MR-TPM is depicted in Fig. 1. The light from a femtosecond laser (Chameleon Ultra II, 700–1000 nm tunable, Coherent) passes through a combination of a half-wave plate and a Glan prism, which can effectively modulate the intensity and polarization direction of the incident light. To use the maximal effective area of the spatial light modulator (SLM) (PLUTO-BB

II,  $1920 \times 1080$  pixels,  $8\text{-}\mu\text{m}$  pixel pitch, 60 Hz, Holoeye Photonics), the size of the incident beam is expanded to 8 mm using a lens pair,  $L_1$  and  $L_2$  ( $f_1 = 30\text{ mm}$ ,  $f_2 = 225\text{ mm}$ ). Next, the first-order beam generated by SLM is passed through lens pair  $L_3$  and  $L_4$  ( $f_3 = f_4 = 175\text{ mm}$ ), which conjugate SLM to a liquid lens (EL-10-30-C-NIR-LD, tuning range  $+5\text{ dpt}$  to  $+10\text{ dpt}$ , control current 0 mA to 290 mA, Optotune). A concave lens ( $f_{OL} = -100\text{ mm}$ ) is used as the offset lens and mounted right after the liquid lens to shift the focal length range to a desired value [21]. Next, the light successively passes through a Galvo  $X$ - $Y$  (TSH8203, 7 mm, Sunny) and the objective (XLUMPLFLN,  $20\times$ , NA=1, Olympus) to form a tight spot in the specimen. The liquid lens, Galvo  $X$ , and Galvo  $Y$  are placed at the conjugate planes of the back pupil of the objective via lens pair  $L_5$  and  $L_6$  ( $f_5 = 125\text{ mm}$ ,  $f_6 = 85\text{ mm}$ ), two doublet pairs  $L_7$  and  $L_8$  ( $f_7 = f_8 = 45\text{ mm}$ ), and a combination of a scan lens (Thorlabs, LSM54-850) and a tube lens ( $f = 200\text{ mm}$ ), respectively. The epi-fluorescence collected from the sample by the objective is reflected by a dichroic mirror (DMLP650R, Thorlabs) and collected by a photomultiplier tube (CH345, Hamamatsu). A National Instruments DAQ card and a Virtual Instrument Software Architecture port are used to control and synchronize the system as well as digitize the signal. In this study, all measurements were performed using an excitation wavelength of 900 nm.

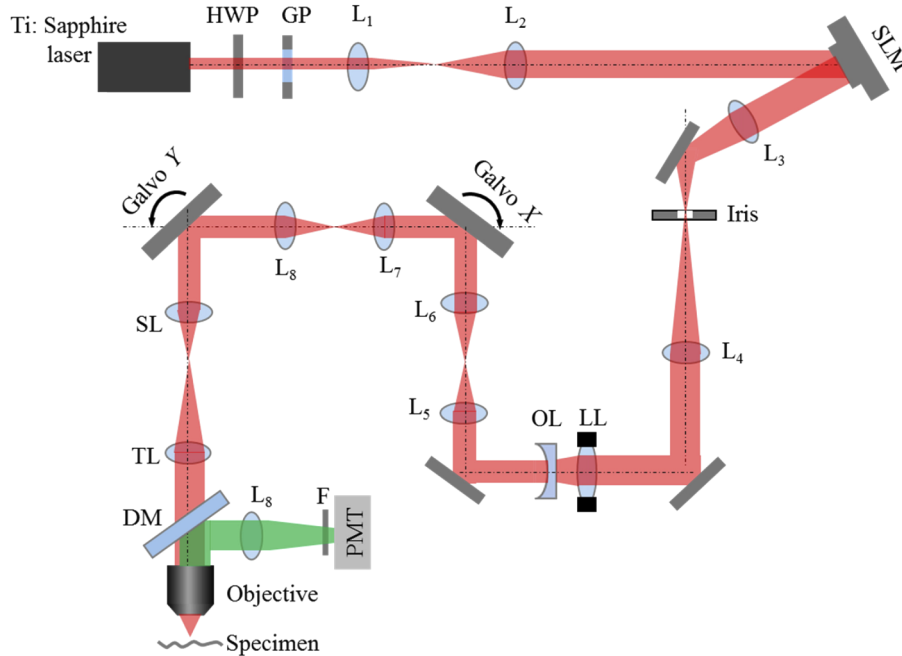


**Fig. 1.** Schematic of optical setup. HWP: half wave plate; GP: Glan prism; L: lens; SLM: spatial light modulator; LL: liquid lens for fast axial scanning; OL: offset lens; Galvo: galvanometric mirror for  $xy$  scanning; SL: scan lens; TL: tube lens; DM: dichroic mirror; F: filter; PMT: photomultiplier tubes. Note that the drawing is not to scale.

## 2.2. Preparation of fluorescent beads

We prepared a gel mixed with 200 nm fluorescent beads (F8811, yellow-green fluorescent (505/515), Thermofisher). The gel was prepared using  $5\text{ }\mu\text{L}$  fluorescent beads and 1 mL 1% agarose solution. The mixture was vortexed vigorously and deposited into a Petri dish. After solidification, the gel was used for imaging.

### 2.3. Preparation of the mouse brain slice

Thy1-GFP-M mice (Stock No. 007788, Jackson Laboratory) were anesthetized deeply, perfused transcardially using phosphate-buffered saline (PBS, pH 7.4), then fixed using 4% paraformaldehyde. Immediately after, the brain was dissected and a 1-mm-thick slice was cut on a freezing microtome. Finally, the brain slice was covered with a coverslip for imaging.

### 2.4. In vivo imaging

**Cranial window:** CX3CR1-GFP mice (Stock No: 005582, Jackson Laboratory) were anesthetized using 4.0% isoflurane inhalation in oxygen for induction and 1.5% to 2.0% for surgery. The fur around the incision site was removed using a hair removal lotion, and the mouse was placed in a stereotaxic frame to secure its head prior to the surgery. The skin on the top of the skull was lifted using forceps, cut using sterile scissors, and removed to expose the skull for craniotomy. Next, a dental drill was used to drill a 3-mm-diameter circle until only a thin layer of the bone remained. Finally, the skull was removed using thin tip forceps, and a metal frame was glued to the skull to fix the head for *in vivo* imaging.

**Cecal ligation and puncture [26]:** (1) The CX3CR1-GFP mice were anesthetized using isoflurane. (2) The lower quadrants of the abdomen were shaved using an electric trimmer and the area was disinfected with alcohol prep pads. (3) A longitudinal skin midline incision was made using a scalpel. (4) The cecum was located using blunt anatomical forceps to isolate and exteriorize it. (5) The cecum was ligated at the designated position for the desired severity grade. (6) The cecum was perforated using one through-and-through puncture midway between the ligation and the tip of the cecum in a mesenteric-to-antimesenteric direction. (7) After removing the needle, a small amount (droplet) of feces was extruded from both the mesenteric and antimesenteric penetration holes to ensure patency. (8) The cecum was relocated into the abdominal cavity without spreading feces onto the abdominal wall wound margins. (9) The peritoneum, fasciae, and abdominal musculature were closed by applying simple running sutures. (10) The skin was closed using metallic clips or by applying simple interrupted sutures.

All the animal experiments were performed in compliance with the protocols approved by the Guangdong Provincial Animal Care and Use Committee and following the guidelines of the Animal Experimentation Ethics Committee of Shenzhen Institutes of Advanced Technology, Chinese Academy of Sciences.

### 2.5. Principle of multi-frame reconstruction two-photon microscopy

The details of the multi-frame super resolution reconstruction are given in Refs. [14–19]. When imaging a real object, the motion between the object and imaging system, the blur effect caused by the PSF of the imaging system, and the down-sampling effect due to the discretization of the imaging sensor inevitably degrade the resolution of the detected image, (see Fig. 2(a)). This process can be represented as

$$P_k = D_k O_k M_k I, k = 1, 2, \dots, n, \quad (1)$$

where  $M_k$ ,  $O_k$ , and  $D_k$  represent, respectively, the motion effect between the real high-resolution image ( $I$ ) and the measured low-resolution volumes ( $P_k$ ), PSF of the imaging system, and the down-sampling effect. The principle governing the proposed MR-TPM is an inverse of the aforementioned process.

First, using two-photon excitation, the object is oversampled along the  $Z$  direction to acquire a raw image stack ( $P$ ). As depicted in Fig. 2(b), ( $P$ ) can be divided into a number of low-resolution two-photon volumes ( $P_k$ ). In each  $P_k$ , the voxel depth ( $d$ ) is set as  $1/3$ – $1/2$  of the axial resolution of the imaging system to satisfy the Nyquist sampling principle. The number of low-resolution volumes,  $n$ , is determined by dividing  $d$  by  $l$ . It indicates that these  $n$  volumes are correlated

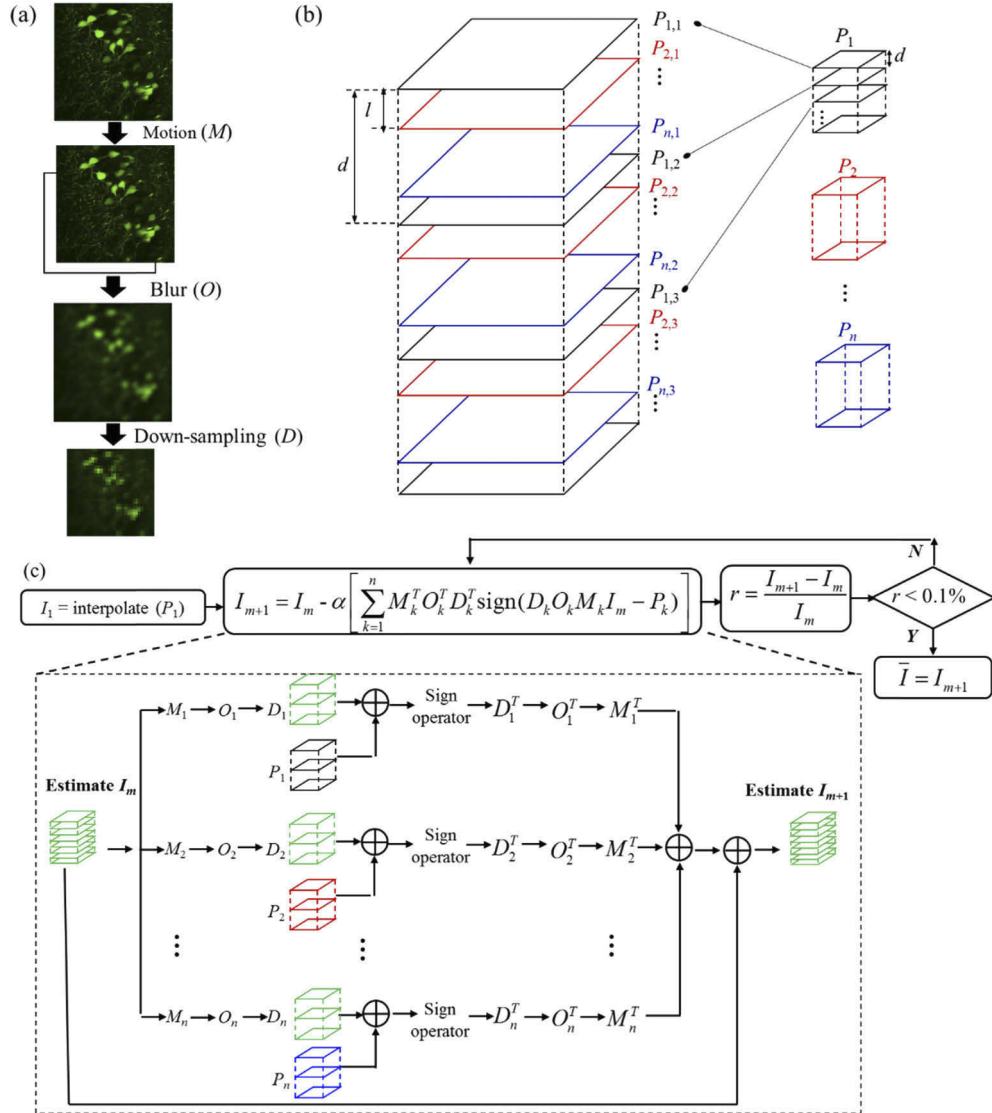


**Fig. 2.** Principle of multi-frame reconstruction two-photon microscopy (MR-TPM). (a) Degradation effects of imaging process. (b) Measurement strategy to acquire a number of axially related low-resolution two-photon volumes. (c) Iterative process to obtain a high-resolution estimate.

with each other in terms of the axial displacement. Typically,  $n$  is chosen as 4 to ensure both the reconstruction accuracy and efficiency (Supplementary Note 1 and Supplementary Fig. S1).

Next, the objective is to search a high-resolution estimate ( $\bar{I}$ ). After processed by the motion operator, the blur operator, and the down-sampling operator, the estimate  $\bar{I}$  is most consistent with multiple measurements ( $P_k$ ). This can be expressed by solving the following minimization problem:

$$\bar{I} = \text{ArgMin} \left[ \sum_{k=1}^n \rho(P_k, D_k O_k M_k I) \right], \quad (2)$$

where  $\rho$  denotes the difference between the degraded  $I$  and  $P_k$ . In this study,  $M_k$ , which implies the axial movement, can be obtained through the known parameters as follows:

$$M_k = (k - 1) \times l. \quad (3)$$

Convolution  $O_k$  uses a measured PSF from a diffraction-limited point source. The down-sampling effect is performed by choosing the slice with an interval of  $d$  for degrading the axial dimension to the level of the low-resolution volume.

Figure 2(c) details the iterative process for calculating  $\bar{I}$ : (i) Create an initial estimate ( $I_1$ ). Interpolate one of the low-resolution volumes, e.g.  $P_1$ , to fill the axial dimension of the high-resolution volume by a factor of  $n$ . (ii) Calculate the next estimate  $I_{m+1}$  ( $m$  denotes the iteration) using the steepest descent method, as shown in the dashed box in Fig. 2(c). Firstly, the warped, blurred, and decimated estimate ( $I_m$ ) is compared with each measurement  $P_k$  in a low-resolution grid. Then, the differences are processed by the inverse operations ( $M_k^T, O_k^T, D_k^T$ ), summed and weighted by a factor of  $\alpha$  to calculate the next estimate ( $I_{m+1}$ ) in a high-resolution grid.  $M_k^T, O_k^T, D_k^T$  are, respectively, the inverse operations of  $M_k, O_k$ , and  $D_k$ . The deconvolution ( $O_k^T$ ) of PSF is based on maximum likelihood estimation, whereas  $M_k^T$  can be obtained through interpolation. (iii) Repeat the iterative process until the difference between  $I_{m+1}$  and  $I_m$  is less than 0.1%. Typically, the convergence rate in this study is 10-20 iterations.

### 3. System characterizations

The aberrations introduced by the optical system limit the achievable axial resolution of TPM, particularly with the liquid lens as the axial scanning engine. Some studies have suggested that the optical aberrations vary when focusing the liquid lens, which degrades the imaging quality [20]. A sensorless AO [23–25] provides a robust way to assess the aberrations introduced by the optical setup, because in this scheme the aberration measurement and correction share a common optical path. The sensorless AO can be regarded as a mathematical optimization problem whose purpose is to maximize image-quality metric. Metric is a function of input parameters that determine the aberration applied by the adaptive element. It reaches a maximum when minimizing the total aberration of the system.

In this study, an iterative method was used to obtain the optimized coefficients of the aberration modes by measuring a uniform fluorescence slice. Furthermore, the average image intensity was chosen as the metric function, and Zernike polynomials, given by Eq. (4), were used as the basic aberration modes to express an arbitrary wavefront, because they form a complete, orthogonal set of functions defined over a unit circle:

$$\varphi(r, \theta) = \sum_{i=1}^n a_i Z_i(r, \theta), \quad (4)$$

where  $\varphi$ ,  $r$ ,  $\theta$ ,  $a_i$ , and  $Z_i$  are the wavefront, polar radius, polar angle, coefficient of each Zernike polynomial, and the corresponding Zernike polynomials, respectively. Table 1 lists the applied Zernike polynomials. Owing to the orthogonal nature of the Zernike polynomials, the optimization



of each Zernike mode can be performed independently. For each applied Zernike polynomial, the coefficient was changed from  $-3$  to  $3$  with an increment of  $0.1$ , and the corresponding pattern was loaded successively using SLM. Subsequently, the images excited from a uniform fluorescence slice were collected to obtain the optimized coefficient that maximizes the average image intensity. Three repeated measurements were performed to ensure the compensation accuracy. The superposition of all the calculated Zernike modes represents the overall aberration of the developed TPM system and is loaded using SLM in practical measurements to minimize the optical aberrations.

**Table 1. Applied Zernike polynomials in this study**

Index ( $i$ )	Zernike polynomials ( $Z_i$ )	Name
1	$\sqrt{6}r^2 \cos 2\theta$	45° astigmatism, 1st
2	$\sqrt{6}r^2 \sin 2\theta$	0° astigmatism, 1st
3	$2\sqrt{2}r^3 \cos 3\theta$	Trefoil
4	$2\sqrt{2}(3r^2 - 2r) \cos \theta$	Coma $X$
5	$2\sqrt{2}(3r^2 - 2r) \sin \theta$	Coma $Y$
6	$2\sqrt{2}r^3 \sin 3\theta$	Trefoil
7	$\sqrt{10}r^4 \cos 4\theta$	Quadrafoil
8	$\sqrt{10}(4r^4 - 3r^2) \cos 2\theta$	45° astigmatism, 2nd
9	$\sqrt{10}(4r^4 - 3r^2) \sin 2\theta$	0° astigmatism, 2nd
10	$\sqrt{10}r^4 \sin 4\theta$	Quadrafoil
11	$\sqrt{5}(6r^4 - 6r^2 + 1)$	Spherical aberration

As a shape-changing lens, the applied liquid lens consists of a container filled with an optical fluid and sealed off with an elastic polymer membrane. With an electromagnetic actuator to exert pressure on the container, the focal length of this liquid lens is accordingly tuned to a desired value within milliseconds using the current flowing through the coil of the actuator. Theoretically, the full axial scanning range of the developed system can be calculated using geometrical optics as [20,27]

$$\Delta z = \frac{1}{R} \frac{f_5^2}{f_{res}} n, \quad (5)$$

where  $R$  denotes the magnification from the focal plane of  $L_5$  to the sample plane right after the liquid lens module;  $n$  is the refractive index of the immersion medium;  $f_5$  and  $f_{res}$  are, respectively, the focal lengths of lens  $L_5$  and the combination of the liquid lens and offset lens, which can be calculated as

$$\frac{1}{f_{res}} = \frac{1}{f_{LL}} + \frac{1}{f_{OL}}, \quad (6)$$

where  $f_{LL}$  and  $f_{OL}$  are the focal lengths of the liquid lens and offset lens, respectively. The theoretical axial scanning range is calculated to be  $104.5 \mu\text{m}$ .

The practical focusing behavior of the liquid lens is calibrated using a high-accuracy mechanical Z-stage (P-737, PI) by measuring 200-nm fluorescent beads. To build the relationship between the focusing behavior of the liquid lens and the axial shift of Z-stage, we imaged one lateral section of fluorescent beads and refocused the same section by the mechanical Z-stage after inputting a current of the liquid lens. Figure 3(a) depicts the results of the theoretical calculation and practical calibration. An almost linear relationship between the remote focusing of the liquid lens and mechanical scanning is evident, which is consistent with the theoretical calculation. Using the developed TPM system, a ratio of  $0.38 \mu\text{m}/\text{mA}$  is calculated and the axial scanning range is  $110 \mu\text{m}$ . It is noted that the practical axial scanning range can be adjusted easily by changing the focal length of the offset lens or the ratio of the relay lens pair.

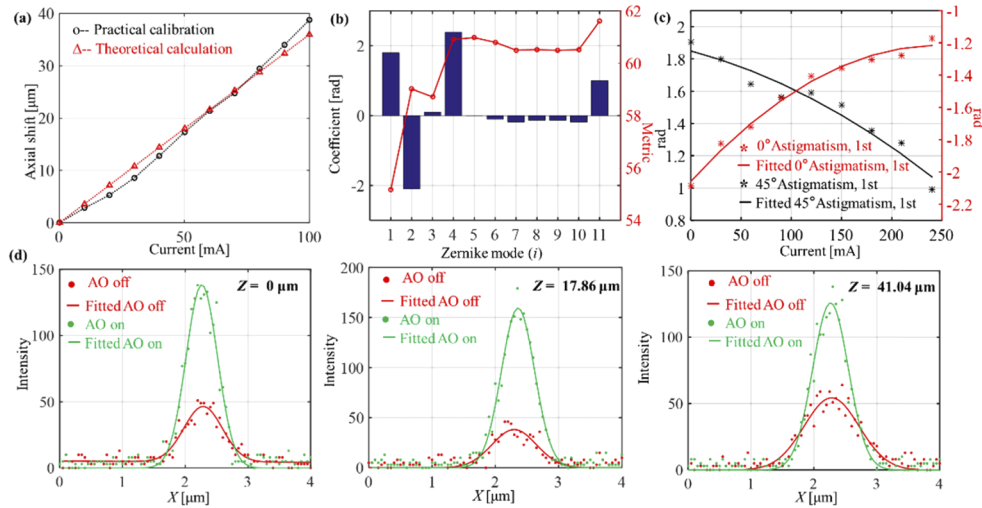


**Fig. 3.** System characterizations. (a) Theoretical and practical focusing behaviors of the liquid lens, calibrated using a mechanical Z-stage. (b) The measured Zernike coefficients (blue bar graph) of the TPM system when the current input of liquid lens is set 0 and the merit values (red line graph) after the correction of each Zernike term. (c) Measured astigmatism under variable current input of liquid lens. (d) Lateral intensity comparisons between AO off and AO on for the same bead at different depths adjusted by the liquid lens.

Then, using the sensorless AO, we measured the wavefront of the developed TPM system when the current input of the liquid lens is set 0. As shown in Fig. 3(b), the measured Zernike coefficients were shown as blue bar graph, while the merit values after the correction of each Zernike term were plotted as red line graph. It is found that the merit values increased after the correction of astigmatism, coma  $Y$  and spherical aberration. The large coma  $Y$  can be explained by the orthogonality of the vertically mounted liquid lens and horizontal optical axis. As the membranes of the liquid lens are elastic, the shape of the lens is influenced by gravity. Other aberrations listed in Table 1 are negligible ( $<0.2$  rad). The RMS error of the overall wavefront of the developed TPM system is in the order of  $0.2\lambda$  (measured at  $\lambda = 900$  nm).

Next, we applied different currents of the liquid lens and measured the corresponding wavefronts. Except the astigmatism, the measured coefficients of other applied aberrations listed in Table 1 were independent of the change in the current input. The measured astigmatism varied based on the current input, as depicted in Fig. 3(c). The measurements were performed thrice. The trend agrees well with Kayvan's measurement results [19], which were obtained using a Shack-Hartmann wavefront sensor.

Considering the variable astigmatism, the strategy of aberration compensation in this study was to load the relatively measured wavefront patterns based on the current input by the fast-changing SLM. In order to verify the validity of the sensorless AO during the liquid lens focusing, we compared the lateral cross-sections of 200-nm fluorescent beads at different depths, as shown in Fig. 3(d). The results suggest that the sensorless AO can effectively improve the peak intensity of measured fluorescent beads and enhance the lateral resolution during the liquid lens focusing. (Additional data can be found in Supplementary note 2 and Fig. S2)



## 4. Experimental results

### 4.1. Imaging fluorescent beads

The feasibility of the proposed AO MR-TPM was verified by measuring 200-nm fluorescent beads. First, the axial resolution of the developed TPM system (without AO correction and MR algorithm) was measured, which was  $\sim 3.5 \mu\text{m}$ . Next,  $d$  was set as  $1.52 \mu\text{m}$  to satisfy the Nyquist sampling principle, and  $l$  was determined to be  $0.38 \mu\text{m}$  (relative to 1 mA current input of the liquid lens). The measured volume was  $27.3 \times 27.3 \times 45.6 \mu\text{m}^3$  with the  $512 \times 512 \times 120$  pixels, and the entire volume was divided into four axially related low-resolution volumes. Figure 4(a)–(d) depicts the same XY plane with conventional TPM, with MR algorithm, with AO compensation, and with both AO compensation and MR algorithm, respectively. The corresponding XZ sections are presented in Fig. 4(e)–(h), while Fig. 4(i) plots a comparison of the intensity profiles of one lateral cross-section (dashed line in Fig. 4(a)–(d)). It is evident that the sensorless AO can improve both the peak intensity of measured fluorescent beads and the lateral resolution, while the MR algorithm contributes to the enhancement of signal-to-noise ratio (SNR) but has almost no impact on the lateral resolution (Fig. 4(i)). One region of interest (ROI, indicated as the yellow dashed box in Fig. 4(e)–(h)), including two fluorescent beads, is magnified in Fig. 4(j). Figure 4(k) shows a comparison of the intensity profiles of one axial cross-section (dashed line in Fig. 4(j)). From Fig. 4(k), it is found that the sensorless AO can effectively improve the peak intensity of measured fluorescent beads by a factor of  $\sim 3$  and slightly enhance the spatial resolution, which is consistent with the results of Fig. 4(i). Crucially, the axial resolution, which can be evaluated using the full width at half maximum (FWHM), can be improved further using the MR algorithm (indicated as a blue line in Fig. 4(k)). Figure 4(l) describes the statistical axial FWHMs of ten beads through the entire volume. The results suggest that the achievable axial FWHM is improved from  $3.6 \mu\text{m}$  using conventional TPM to  $1 \mu\text{m}$  using the proposed AO MR-TPM without getting affected by the focusing behavior of the liquid lens. (A comparison between the proposed MR algorithm and only deconvolution process was provided in Supplementary note 3 and Fig. S3)

### 4.2. In vitro imaging of mouse brain slice

We validated the practicability of AO MR-TPM further by imaging the brain slice of the Thy1-GFP-M mice. In this experiment,  $l$  was  $0.19 \mu\text{m}$  (relative to 0.5 mA current input of the liquid lens) and  $d$  was  $0.76 \mu\text{m}$ . Cerebral nerve cells were imaged in a volume of  $273 \times 273 \times 38 \mu\text{m}^3$  with  $512 \times 512 \times 200$  pixels, and the entire volume was divided into four axially related low-resolution volumes. The lateral (Max Intensity Project, MIP) and axial (one XZ section) views with conventional TPM are depicted in Fig. 5(a) and (b), whereas Fig. 5(c) and (d) exhibits the same lateral and axial views with the proposed AO MR-TPM. For a clear comparison, we further magnified two ROIs (indicated as purple and blue boxes in Fig. 5(a)) in Fig. 5(e) and (f) with the corresponding axial views of Fig. 5(g) and (h) using conventional TPM. The relative results using the proposed AO MR-TPM are plotted in Fig. 5(i)–(l). It is evident that AO MR-TPM sharpened the image and resulted in axons with a finer apparent width (compare Fig. 5(b) and (d)). The cell bodies and their connection along the axial direction can be seen more clearly with the increased image contrast using AO MR-TPM (compare Fig. 5(g) and (k)). Furthermore, some axon features that cannot be resolved by conventional TPM become distinguishable using the proposed method (compare Fig. 5(h) and (l)).

### 4.3. In vivo imaging of the mouse cerebral microglia

Finally, we provide some results of the *in vivo* imaging of the mouse cerebral microglia, a comparison between the conventional TPM and proposed AO MR-TPM, and the observation of changes of microglial cells in the septic mice using AO MR-TPM. As the resident macrophage cells, microglia plays an important role in active immune defense in the central nervous system.

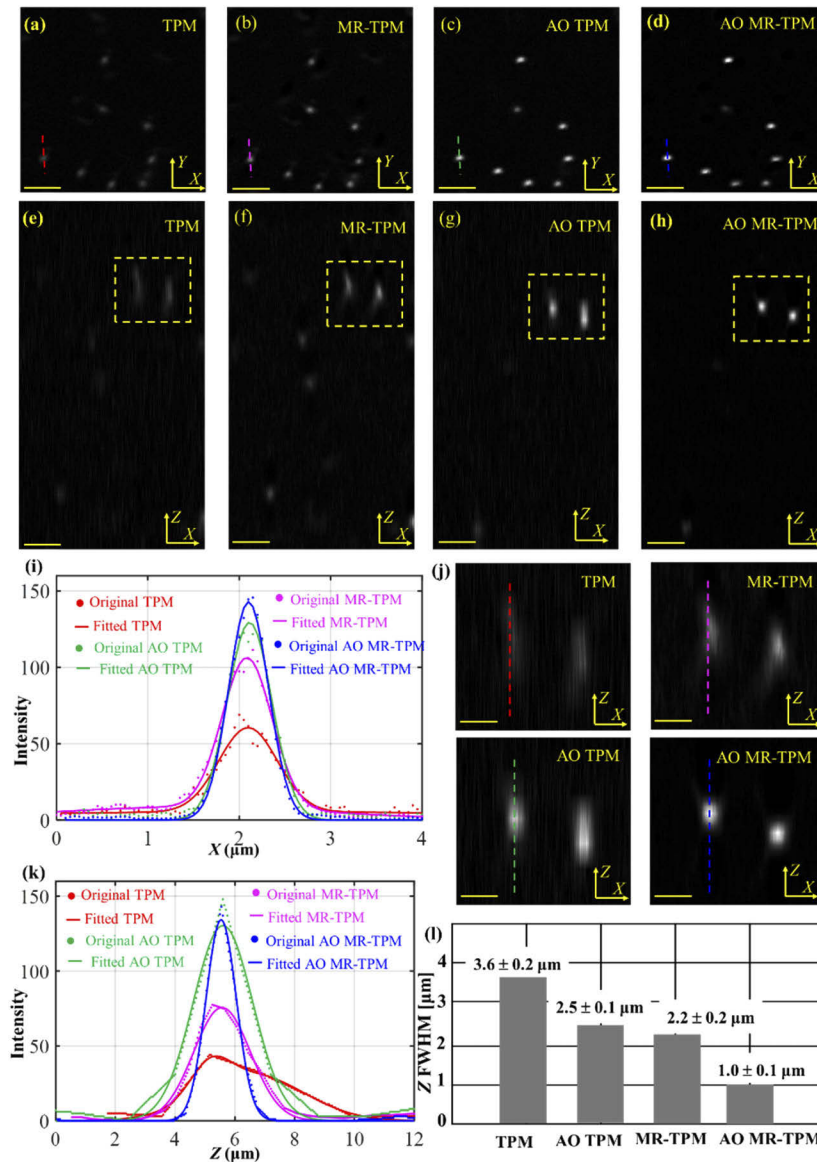


**Fig. 4.** Imaging of 200-nm fluorescent beads. (a–d) The same XY plane without AO compensation, with MR algorithm, with AO compensation, and with both AO compensation and MR algorithm. (e–h) The same XZ section with the four methods. (i) Intensity comparison of one lateral cross-section from (a–d) using the four methods. (j) Magnified ROIs from (e–h). (k) Intensity comparison of one axial cross-section from (j) using the four methods. (l) Statistics of the axial FWHMs of ten beads through the entire volume. Scale bars:  $5 \mu\text{m}$  (a–h),  $2 \mu\text{m}$  (j).

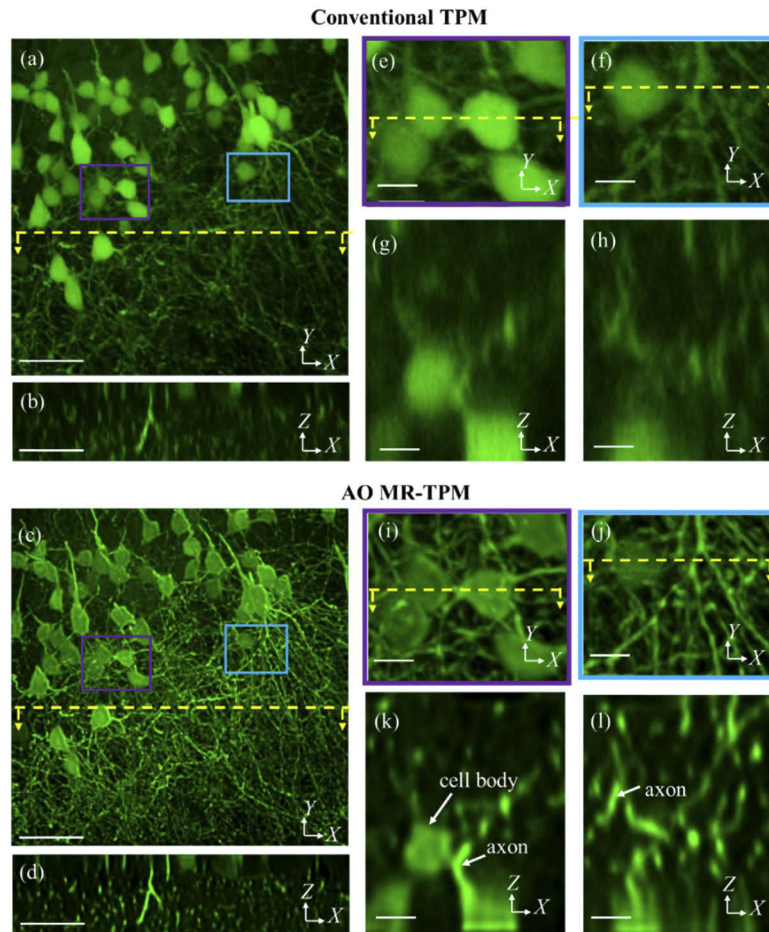


**Fig. 5.** Three-dimensional imaging of neural networks of Thy1-GFP-M mice brain slice. (a, b) Lateral (Max Intensity Project, MIP) and axial (one XZ section) views using conventional TPM. (c, d) Image as in (a) and (b), but with AO MR-TPM. (e, f) Higher magnification views of boxed regions in (a). (g, h) Corresponding axial views of (e, f) (indicated as yellow dashed lines). (i, j) Image as in (e) and (f), but with AO MR-TPM. (k, l) The corresponding axial views of (i, j) (indicated as yellow dashed lines). Scale bars: 50  $\mu\text{m}$  (a, b, h, i), 10  $\mu\text{m}$  (c–f, j–m).

In both the experiments,  $l$  was  $0.19\ \mu\text{m}$  (relative to  $0.5\ \text{mA}$  current input of the liquid lens) and  $d$  was  $0.76\ \mu\text{m}$ . The microglial cells were imaged in a volume of  $273 \times 273 \times 38\ \mu\text{m}^3$  with  $512 \times 512 \times 200$  pixels.

Figure 6(a) depicts the lateral view (MIP) of the measured volumes using the conventional TPM, whereas the lateral view using the AO MR-TPM is presented in Fig. 6(b). For a better comparison, four ROIs of various  $XZ$  sections (indicated as arrowed and dashed lines in Fig. 6(a) and (b)) are magnified in Fig. 6(c)–(f) using the conventional TPM and in Fig. 6(g)–(j) using the AO MR-TPM. Figure 6(k) depicts the plots of the line-outs of microglial cells marked in the white line in Fig. 6(e) and in the red line in Fig. 6(i), whereas the line-outs of microglial cells marked in the white line in Fig. 6(f) and the red line in Fig. 6(j) are illustrated in Fig. 6(l). Evidently, AO MR-TPM sharpened the image and resulted in a process of microglia with a finer

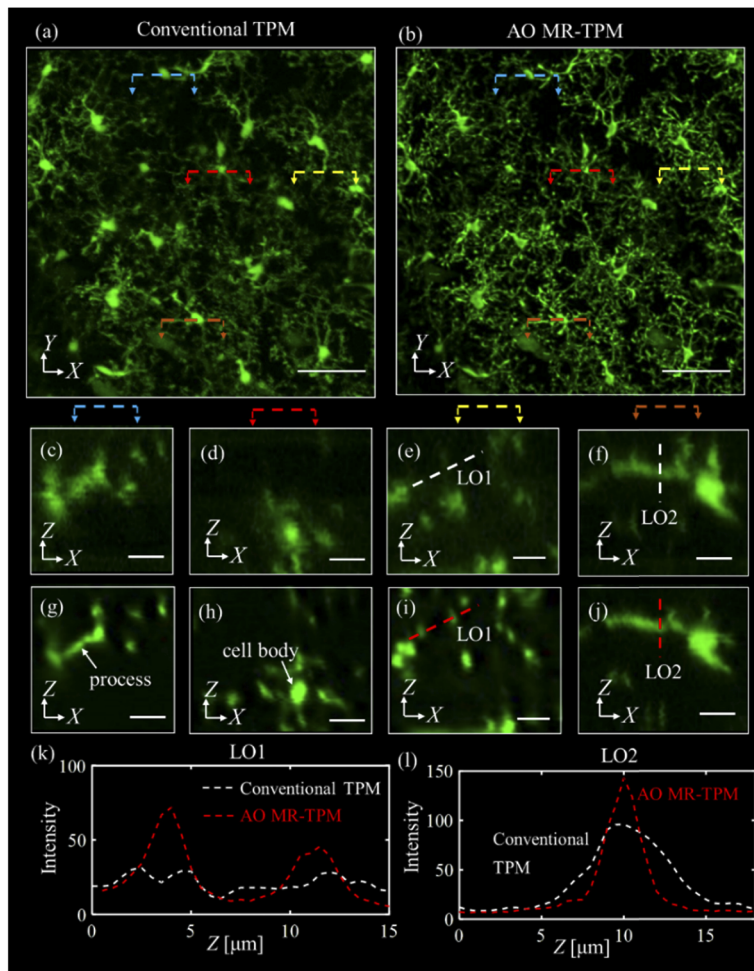


**Fig. 6.** *In vivo* imaging of the mouse cerebral microglia. (a) Lateral view (MIP) using conventional TPM. (b) Image as in (a), but with AO MR-TPM. (c–f) Four ROIs of various  $XZ$  sections (indicated as arrowed and dashed lines in (a)) using conventional TPM. (g–j) The corresponding ROIs (indicated as arrowed and dashed lines in (b)) using AO MR-TPM. (k) Line-outs of microglial cells marked in the white line in (e) and red line in (i). (l) Line-outs of microglial cells marked in the white line in (f) and red line in (j). Scale bars:  $50\ \mu\text{m}$  (a, b),  $10\ \mu\text{m}$  (c–j).



apparent width along the axial direction (Fig. 6(c, f, g, j, l)). Improvements in both the peak intensity and axial resolution can be observed by imaging the axial line-outs of the process of microglia (Fig. 6(l)). Furthermore, the indiscernible process of the microglia (Fig. 6(d, e)) along the axial direction using the conventional TPM can be clearly resolved by our proposed method (Fig. 6(h, i, k)). The results indicate that the AO MR-TPM can effectively improve the axial resolution with a higher SNR when compared with the conventional TPM for *in vivo* imaging, similar to the effect in *in vitro* imaging.

Figure 7 depicts the dynamic measurement of microglial cells of the septic mice. It is known that the cecal ligation and puncture in septic mice induce microglial trafficking to sites adjacent to leukocyte adhesion on inflamed cerebral microvessels [28]. Figure 7(a) is a lateral view of the entire volumes using the proposed AO MR-TPM at a certain time. Figure 7(b)–(d) shows a magnified ROI (indicated as a red dashed box in Fig. 7(a)) with the corresponding axial views (indicated as white lines in Fig. 7(b)–(d)) at various times. Another magnified ROI at various times is depicted in Fig. 7(e)–(g). The time interval is 20 min. The 3D morphological changes in microglial cells can be monitored. In particular, the collapse of the process toward the cell body along the axial direction can be observed clearly. Our technology may provide a useful tool to analyze 3D microglial overactivation during septic encephalopathy.

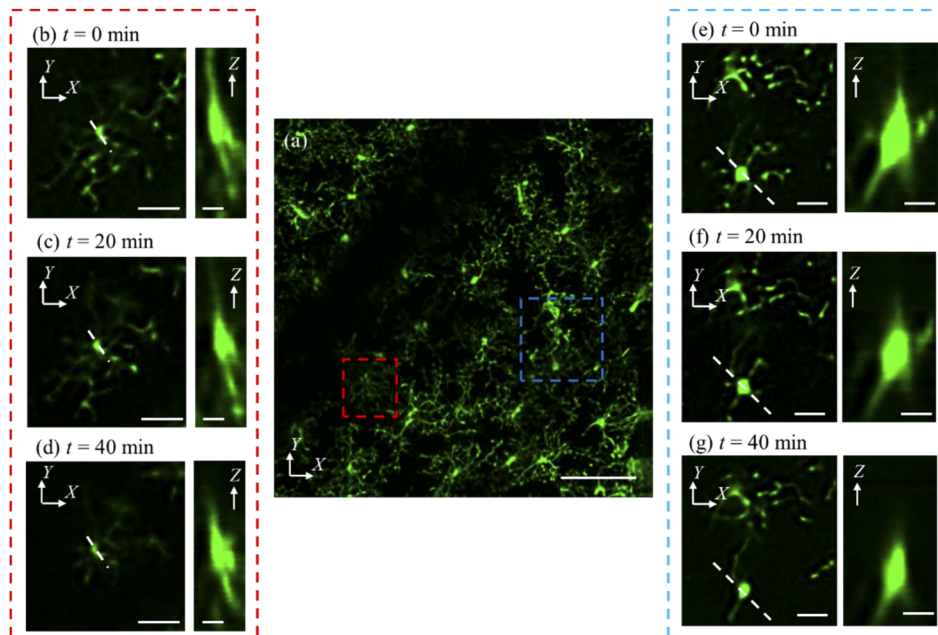


**Fig. 7.** Dynamic measurement of microglial cells in septic mice using AO MR-TPM. (a) Lateral view (MIP) at a certain time. (b–d) A magnified ROI (indicated as the red dashed box in (a)) with corresponding axial view (indicated as white lines in lateral views of (b–d)) at various times. (e–g) Another magnified ROI (indicated as the blue dashed box in (a)) with corresponding axial view (indicated as white lines in lateral views of (e–g)) at various times. Scale bars: 50  $\mu\text{m}$  (a), 20  $\mu\text{m}$  (lateral views of (b–g)), 10  $\mu\text{m}$  (axial views of (b–g)). Time interval between (b–d) or (e–g) is 20 min.

## 5. Discussion and conclusion

In this study, we proposed and implemented a MR-TPM combined with a sensorless AO and liquid lens. The proposed method enables almost threefold enhancement of the axial resolution

and higher SNR relative to the conventional TPM. Moreover, this technology is compatible with the conventional TPM and requires no sophisticated design of excitation paths or optical post-processing. The feasibility of our method was demonstrated by imaging fluorescent beads, neural circuit of mouse brain slice, and cerebral microglia of live mouse. The proposed AO MR-TPM can clearly resolve some fine features, such as the axon in the neural circuit and the process of microglial cells along the axial direction, which are indistinguishable using the conventional TPM. In addition, our method can be used to monitor the 3D morphological changes in microglial cells in septic mice.

Compared with the conventional TPM, AO MR-TPM can effectively enhance the axial resolution by suppressing the effect of optical aberrations, inadequate sampling, and poor focusing capability. The principle of MR-TPM comprises two aspects: (1) collecting a number of axially related low-resolution two-photon volumes and (2) estimating a high-resolution output by reversing the process of motion, blur, and down-sampling based on the steepest descent method and maximum likelihood estimation. Theoretically, if the oversampling step and PSF of an optical system can be determined accurately, the principle of multi-frame reconstruction can be applied to improve the spatial resolution of other far-field imaging methods, e.g., wide-field imaging or confocal microscopy.

Using a liquid lens as the fast axial scanning engine can alleviate the problem of low measurement efficiency caused by oversampling in MR-TPM. In our work, the overall imaging time is approximately 5 minutes for a volume of  $512 \times 512 \times 120$  pixels. The 3D imaging rate is limited by the lateral scan speed of galvanometric mirrors rather than the settling time of the liquid lens. If high-speed scanners, e.g., resonant mirrors, are used, fast high-resolution volumetric two-photon imaging can be expected, which is a future study for us.

The proposed technology can broaden the application of TPM in 3D biological explorations, particularly in neurosciences because of the significance of understanding the structure and function of neural circuits. It is known that the neural circuit is a population of neurons interconnected by 3D distributed dendrites, axons, and synapses. Their minimal diameters are of the submicron order. In this study, a  $20\times$  NA=1 objective was used and 1- $\mu\text{m}$  axial resolution was achieved. If a higher NA objective is applied in AO MR-TPM, the proposed method has the potential to provide submicron resolving power along the axial direction together with a higher SNR.

## Funding

National Key Research and Development Program of China (2017YFC0110200); National Natural Science Foundation of China (81701744, 81822023, 81927803, 91959121, 21874052, 21927802); Natural Science Foundation of Guangdong Province (2017A030310308, 2020B121201010); Guangdong Basic and Applied Basic Research Foundation (2019A1515011746); Scientific Instrument Innovation Team of Chinese Academy of Sciences (GJJSTD20180002); Shenzhen Basic Research Program (JCYJ20170818164343304, JCYJ20180507182432303, ZDSY20130401165820357).

## Acknowledgement

We thank Dr. Yang Zhan at Brain Cognition and Brain Disease Institute for providing the Thy1-GFP-M mice. We thank Dr. Bo Peng at Institute for Translational Brain Research for providing the CX3CR1-GFP mice

## Disclosures

The authors declare no conflicts of interest.



See [Supplement 1](#) for supporting content.

## References

- W. Wang and R. Yuste, "In vivo imaging of neural activity," *Nat. Methods* **14**(4), 414–416 (2017).
- N. Ji, J. Freeman, and S. L. Smith, "Technologies for imaging neural activity in large volumes," *Nat. Neurosci.* **19**(9), 1154–1164 (2016).
- E. E. Hoover and J. A. Squier, "Advances in multiphoton microscopy technology," *Nat. Photonics* **7**(2), 93–101 (2013).
- C. J. R. Sheppard and M. Gu, "Image-formation in 2-photon fluorescence microscopy," *Optik* **86**, 104–106 (1990).
- W. R. Zipfel, R. M. Williams, and W. W. Webb, "Nonlinear magic: multiphoton microscopy in biosciences," *Nat. Biotechnol.* **21**(11), 1369–1377 (2003).
- U. Böhm, S. W. Hell, and R. Schmidt, "4Pi-RESOLFT nanoscopy," *Nat. Commun.* **7**(1), 10504 (2016).
- S. Glaschick, C. Rucker, K. Deuschle, J. Wiedenmann, F. Oswald, V. Mailänder, and G. U. Nienhaus, "Axial resolution enhancement by 4Pi confocal fluorescence microscopy with Two-Photon Excitation," *J. Biol. Phys.* **33**(5-6), 433–443 (2007).
- G. Moneron and S. W. Hell, "Two-photon excitation STED microscopy," *Opt. Express* **17**(17), 14567–14573 (2009).
- P. Bethge, R. Chéreau, E. Avignone, G. Marsicano, and U. V. Nägerl, "Two-photon excitation STED microscopy in two colors in acute brain slices," *Biophys. J.* **104**(4), 778–785 (2013).
- C. B. Müller and J. Enderlein, "Image scanning microscopy," *Phys. Rev. Lett.* **104**(19), 198101 (2010).
- M. Ingaramo, A. G. York, P. Wawrzus, O. Milberg, A. Hong, R. Weigert, H. Shroff, and G. H. Patterson, "Two-photon excitation improves multifocal structured illumination microscopy in thick scattering tissue," *Proc. Natl. Acad. Sci.* **111**(14), 5254–5259 (2014).
- P. W. Winter, A. G. York, D. D. Nogare, M. Ingaramo, R. Christensen, A. Chitnis, G. H. Patterson, and H. Shroff, "Two-photon instant structured illumination microscopy improves the depth penetration of super-resolution imaging in thick scattering samples," *Optica* **1**(3), 181–191 (2014).
- W. Zheng, Y. Wu, P. Winter, R. Fischer, D. D. Nogare, A. Hong, C. McCormick, R. Christensen, W. P. Dempsey, D. B. Arnold, J. Zimmerberg, A. Chitnis, J. Sellers, C. Waterman, and H. Shroff, "Adaptive optics improves multiphoton super-resolution imaging," *Nat. Methods* **14**(9), 869–872 (2017).
- S. Farsiu, M. D. Robinson, M. Elad, and P. Milanfar, "Fast and robust multiframe super resolution," *IEEE Trans. Image Process.* **13**(10), 1327–1344 (2004).
- M. Elad and Y. Hel-Or, "A fast super-resolution reconstruction algorithm for pure translational motion and common space-invariant blur," *IEEE Trans. Image Process.* **10**(8), 1187–1193 (2001).
- G. Zheng, S. A. Lee, S. Yang, and C. Yang, "Sub-pixel resolving optofluidic microscope for on-chip cell imaging," *Lab Chip* **10**(22), 3125–3129 (2010).
- G. Zheng, S. A. Lee, Y. Antebi, M. B. Elowitz, and C. Yang, "The ePetri dish, an on-chip cell imaging platform based on subpixel perspective sweeping microscopy (SPSM)," *Proc. Natl. Acad. Sci.* **108**(41), 16889–16894 (2011).
- P. Fei, J. Nie, J. Lee, Y. Ding, S. Li, H. Zhang, M. Hagiwara, T. Yu, T. Segura, C. Ho, D. Zhu, and T. K. Hsiai, "Subvoxel light-sheet microscopy for high-resolution high-throughput volumetric imaging of large biomedical specimens," *Adv. Photonics* **1**(1), 016002 (2019).
- J. Nie, S. Liu, T. Yu, Y. Li, J. Ping, P. Wan, F. Zhao, Y. Huang, W. Mei, S. Zeng, D. Zhu, and P. Fei, "Fast, 3D Isotropic Imaging of Whole Mouse Brain Using Multiangle-Resolved Subvoxel SPIM," *Adv. Sci.* **7**(3), 1901891 (2020).
- K. F. Tehrani, C. V. Latchoumane, W. M. Southern, E. G. Pendleton, A. Maslesa, L. Karumbaiah, J. A. Call, and L. J. Mortensen, "Five-dimensional two-photon volumetric microscopy of in-vivo dynamic activities using liquid lens remote focusing," *Biomed. Opt. Express* **10**(7), 3591–3604 (2019).
- B. F. Grewe, F. F. Voigt, M. V. Hoff, and F. Helmchen, "Fast two-layer two-photon imaging of neuronal cell populations using an electrically tunable lens," *Biomed. Opt. Express* **2**(7), 2035–2046 (2011).
- Z. Ding, C. Wang, Z. Hu, Z. Cao, Z. Zhou, X. Chen, H. Chen, and W. Qiao, "Surface profiling of an aspherical liquid lens with a varied thickness membrane," *Opt. Express* **25**(4), 3122–3132 (2017).
- D. Débarre, E. J. Botcherby, T. Watanabe, S. Srinivas, M. J. Booth, and T. Wilson, "Image-based adaptive optics for two-photon microscopy," *Opt. Lett.* **20**(3), 2598–2612 (2012).
- A. Facomprez, E. Beaupaire, and D. Débarre, "Accuracy of correction in modal sensorless adaptive optics," *Opt. Express* **17**(16), 13768–13784 (2009).
- D. J. Wahl, Y. Jian, S. Bonora, R. J. Zawadzki, and M. V. Sarunic, "Wavefront sensorless adaptive optics fluorescence biomicroscope for in vivo retinal imaging in mice," *Biomed. Opt. Express* **7**(1), 1–12 (2016).
- D. Rittirsch, M. S. Huber-Lang, M. A. Flierl, and P. A. Ward, "Immunodesign of experimental sepsis by cecal ligation and puncture," *Nat. Protoc.* **4**(1), 31–36 (2009).
- F. O. Fährbach, F. F. Voigt, B. Schmid, F. Helmchen, and J. Huiskens, "Rapid 3D light-sheet microscopy with a tunable lens," *Opt. Express* **21**(18), 21010–21026 (2013).
- H. Wang, L. Hong, J. Huang, R. Tao, C. Tan, N. Lu, C. Wang, M. M. Ahmed, Y. Lu, Z. Liu, W. Shi, E. Lai, C. S. Wilcox, and F. Han, "P2RX7 sensitizes Mac-1/ICAM-1-dependent leukocyteendothelial adhesion and promotes neurovascular injury during septic encephalopathy," *Cell Res.* **25**(6), 674–690 (2015).